



Scanning vortex microscopy reveals thickness-dependent pinning nanonetwork in superconducting niobium films



Razmik A. Hovhannisyanyan¹, Sergey Yu. Grebenchuk¹, Semen A. Larionov¹, Andrey G. Shishkin^{1,2,3}, Artem K. Grebenko¹, Nadezhda E. Kupchinskaya¹, Ekaterina A. Dobrovolskaya¹, Olga V. Skryabina^{1,4}, Alexey Yu. Aladyshkin^{1,5,6}, Vyacheslav V. Dremov¹, Igor A. Golovchanskiy¹, Alexey V. Samokhvalov^{5,6}, Alexander S. Mel'nikov^{1,5,6}, Dimitri Roditchev⁷ & Vasily S. Stolyarov^{1,2,3,7} ✉

The presence of quantum vortices determines the electromagnetic response of superconducting materials and devices. Controlling the motion of vortices and their pinning on intrinsic and artificial defects is therefore essential for further development of superconducting electronics. Here we take advantage of the attractive force between a magnetic tip of the Magnetic Force Microscope and a single quantum vortex to spatially map the pinning force inside 50–240 nm thick magnetron-sputtered niobium films, widely used in various applications. The revealed pinning nanonetwork is related to the thickness-dependent granular structure of the films as well as to the characteristic microscopic scales of superconductivity. Our approach is general and can be directly applied to other type-II granular superconducting materials and nanodevices.

Defects play a crucial role in superconductivity^{1–4}. In superconducting electronic devices, their presence is often detrimental or unwanted^{5–8}. In other applications, such as superconducting wires and cables, defects enable the pinning of Abrikosov vortices, thus enhancing the critical current density^{9,10}. Moreover, disordered superconducting films have high kinetic inductance^{11,12}, making them promising for applications in superconducting quantum devices and sensors¹³.

The physics of the vortex-defect interaction in type-II superconductors is also a very important fundamental problem¹⁴. For several decades different scenarios of individual and collective vortex pinning have been studied including pinning on columnar defects¹⁵, blind holes¹⁶, non-superconducting inclusions¹⁷, magnetic particles^{2,18}, among others (see ref. 19 for a review). Basic mechanisms of the vortex trapping on defects are related either to the changes in the energy of supercurrents²⁰ or vortex-core energy¹⁴. The progress in technology enables tuning and controlling the vortex pinning using the sample thickness modulation²¹, substrate engineering²², surface decoration with magnetic nanoparticles²³, engineering of the specific pinning centers²⁴, and ion irradiation²⁵.

A detailed knowledge of the pinning network parameters is deeply desired in all cases. However, their experimental studies are very challenging, as even tiny non-magnetic defects such as grain boundaries or non-

superconducting inclusions could serve as efficient pinning centers on the scale of the superconducting coherence length. This covers spatial scales ranging from a few nanometers to several microns. Thus, an ideal probe should (i) have a nanoscale resolution combined with a large field of view, (ii) be sensitive to both bulk and surface defects, and (iii) be non-destructive.

Various microscopies enable nanometer-scale defect imaging. Transmission electron microscopy offers the analysis down to atomic scale^{26,27}, but it is destructive and probes a tiny part of the sample. Scanning probe methods such as electron microscopy²⁸, tunneling^{29,30}, and atomic force microscopy³¹ also show excellent spatial resolution and are non-destructive. Yet, they only reveal defects that protrude at the surface (e.g., cracks, voids or grain boundaries) and provide only limited information about the pinning efficiency of those defects. More dedicated methods probe specific superconducting properties. Magneto-optical imaging³², Lorentz microscopy³³, magnetic (Bitter) decoration³⁴, scanning SQUID^{–35,36}, scanning Hall-probe^{–37} and magnetic force microscopies (MFM)^{38–41} probe spatial variations of the magnetic field outside the sample. These methods enable retrieving the distribution of screening (Meissner) and transport currents in the material. Low-temperature scanning laser^{–42,43} and scanning electron microscopies⁴⁴ probe thermal processes in superconductors subject to local heating by a focused laser

¹Moscow Institute of Physics and Technology, Dolgoprudny, Russia. ²Dukhov Research Institute of Automatics (VNIIA), Moscow, Russia. ³National University of Science and Technology MISIS, Moscow, Russia. ⁴Institute of Solid State Physics RAS, Chernogolovka, Russia. ⁵Institute for Physics of Microstructures RAS, Nizhny Novgorod, Russia. ⁶Lobachevsky State University of Nizhny Novgorod, Nizhny Novgorod, Russia. ⁷LPEM, UMR-8213, ESPCI Paris, PSL, CNRS, Sorbonne University, Paris, France. ✉e-mail: stolyarov.vs@phystech.edu

beam⁴⁵. These techniques are non-destructive and access the bulk properties, thus providing useful information about the characteristics of superconducting cables^{35,38} and devices^{4,40,42–44,46}. However, these approaches have spatial resolution typically in the range of microns, thus missing nanoscale defects. Therefore, the quest for high-resolution, non-destructive method of defect network characterization in superconductors is still open.

In the present work, we study the spatial and temperature evolution of the vortex pinning in magnetron-sputtered 50–240 nm thick Nb films, which are widely used in superconducting electronics and quantum technology^{4,13,47–51}. We use the magnetic tip located at the oscillating MFM cantilever to generate a single quantum vortex in the studied sample upon its cooling below the superconducting critical temperature T_c . Once created, the vortex is attracted to the MFM tip. In the experiment, the tip is scanned over the studied region of the film and drags the vortex, which explores the superconducting sample by jumping from one pinning center to the other. These successive jumps are detected through the modifications of vortex-cantilever force³⁸ and are presented in the form of spatial maps.

Since the vortex pinches through the whole thickness of a superconductor, it is the bulk pinning potential that is probed, and its spatial distribution, projected to 2D-maps, is obtained in this non-destructive Scanning Quantum Vortex Microscopy (SQVM) experiment. Surprisingly, the SQVM demonstrated a very high spatial resolution of about ~ 20 nm, at least one order of magnitude better than the expected limitation (~ 250 nm) due to the lateral extent of the vortex-cantilever magnetic interaction, at the used experimental conditions. We put forward theoretical arguments to

show that the spatial resolution of SQVM is controlled by the superconducting coherence length and not by the extent of the magnetic interaction. Furthermore, a comparison between the SQVM maps and Atomic Force Microscopy (AFM) images enabled us to relate the pinning network to the granular structure of the films, and to conclude that the microscopic origin of the vortex pinning there is the vortex core blocking by the grain boundaries.

Results

The studied Nb films were deposited onto the silicon substrate using a standard magnetron sputtering (see Section Sample Preparation in Methods and refs. 29,39 for comprehensive details). The properties of these commonly used films have been extensively studied in the past several works focused on vortex pinning on both intrinsic and artificial defects^{6,8,41,47,48}. The films are known to exhibit strong vortex pinning on structural defects formed during deposition^{52,53}.

Figure 1 a represents a typical AFM image acquired at room temperature on the surface of a 100-nm-thick Nb-film. The inset is a $0.5 \times 0.5 \mu\text{m}^2$ zoom on the same sample area. The granular structure of the film is clearly revealed: the grains appear elongated with the apparent length ~ 30 – 50 nm and width ~ 5 nm^{54,55}. The grain boundaries are tiny and are not resolved. Remarkably, the neighboring grains are co-aligned, forming larger ~ 30 – 50 nm^2 clusters separated by voids appearing as elongated dark spots (see Supplementary Figs. 1 and 2).

To realize the vortex pinning maps by SQVM, the first step is to create an interacting nano-probe: a single Abrikosov vortex, in the present case. To

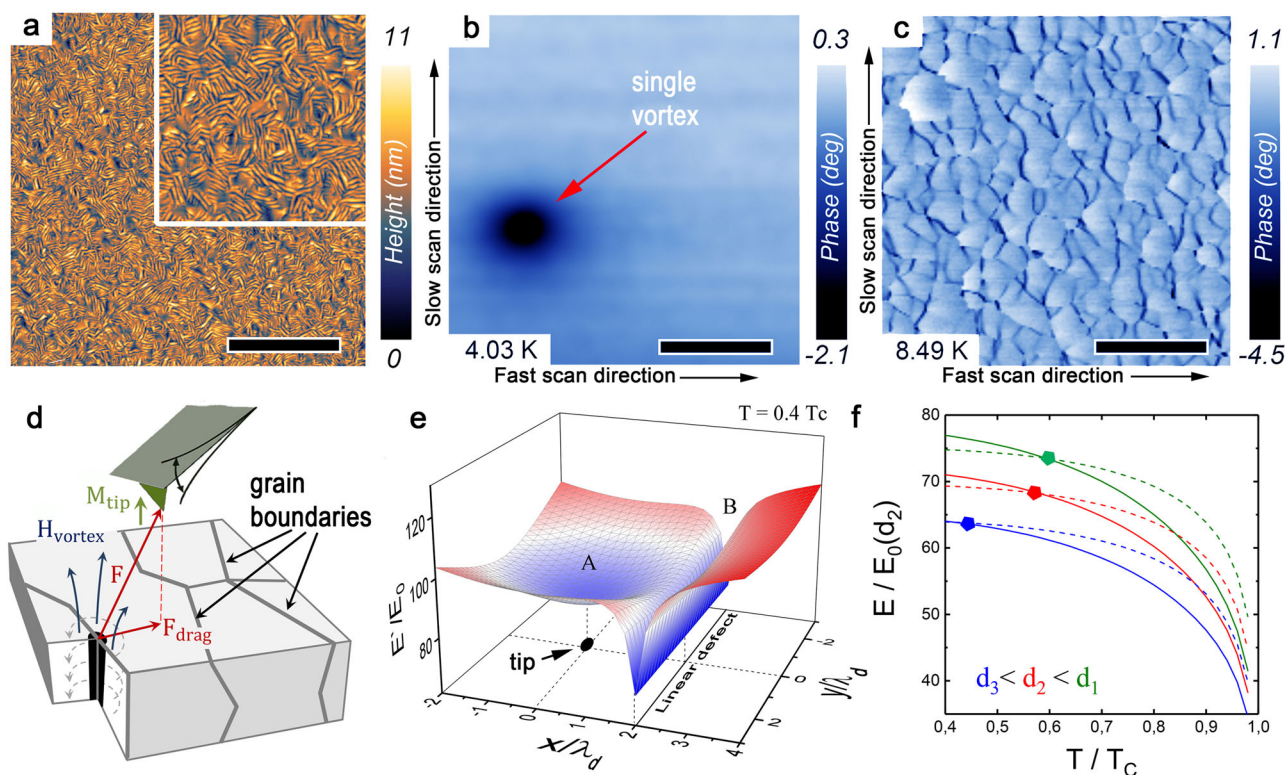


Fig. 1 | Principles of SQVM. a Room-temperature AFM $3 \times 3 \mu\text{m}^2$ image of a 100-nm-thick Nb film. The inset represents $0.5 \times 0.5 \mu\text{m}^2$ zoom on the sample surface (refer to the Methods section concerning High resolution AFM measurements). **b** MFM and **c** SQVM $3 \times 3 \mu\text{m}^2$ images of 100-nm-thick film acquired at $T = 4.03$ and 8.49 K, respectively. The black scale bar in panels a–c corresponds to $1 \mu\text{m}$. **d** sketch of the SQVM experiment. Vortex currents (gray dashed arrows) circulate around the vortex core (black cylinder) pinned at a defect (dark gray). The vortex currents produce a non-uniform magnetic field $\mathbf{H}_{\text{vortex}}$ interacting (a force \mathbf{F}) with the magnetic moment \mathbf{M}_{tip} of the oscillating MFM cantilever (green). During scanning, the misalignment between the vortex and the cantilever results in a drag force \mathbf{F}_{drag}

which tends to unpin the vortex from the defect. When the drag force exceeds the pinning one, the vortex follows the MFM tip and 'draws' the pinning network. **e** spatial variation of the normalized free energy as a function of the vortex position calculated for $T = 0.4 T_c$ (see definitions in the text). The cantilever apex is located at the point A, and the linear defect in B. **f** temperature dependence of the normalized free energy for the vortex located under the cantilever in A (solid lines) and the defect in B (dashed lines). The blue, red and green curves correspond to the sample thicknesses $d = 50, 100$, and 240 nm, respectively. The crossover temperature T^* marked by closed pentagons depends on the film thickness and the thickness-dependent magnetic penetration depth λ_d (see also open red circles in Fig. 2h).

do so, the samples were placed in cryogenic MFM (refer to the Methods section concerning Cryogenic MFM and SQVM measurements) and cooled below the critical temperature of the superconducting transition $T_c \approx 9.05$ K. During the cooling process, the Co/Cr magnetic tip of the MFM cantilever was kept above the sample surface at a height (lift) of ~ 2 μm . At this lift, the stray magnetic field of the tip piercing the sample is only a few Oe; though, this field is enough to create one or a few magnetic flux quanta in the area of interest. Below T_c , this magnetic flux becomes quantized in the form of a single vortex. Note that, in general, even zero-field cooled samples may freeze some quantum vortices due to the magnetic field of the Earth. While these vortices can also be used for SQVM, their initial location is uncontrolled.

Figure 1b displays a 3×3 μm^2 MFM map of the film acquired in the area where the quantum vortex was expected to be created at $T = 4.03$ K (well below $T_c^{100\text{nm}} = 9.0$ K, cantilever lift is 200 nm). Note that in all presented images, the horizontal axis follows the direction of the fast scan. In this image, the gray contrast represents the phase shift of the MFM cantilever oscillations. The phase shift $\delta\theta$ is proportional to the spatial derivative of the force experienced by the cantilever along the oscillation direction; the latter is normal to the surface (see Eq. (1) below). The phase shift is positive for the repulsive normal forces and negative for the attractive ones. Due to the Meissner diamagnetism, the main interaction between the magnetized cantilever and the film in the absence of the vortex is repulsive; it is witnessed by a positive phase shift measured on most of the scanned area. However, a spot – a single Abrikosov vortex – is observed near the left edge of the image. The cantilever created this vortex during cooling when the sample became superconducting. The spot appears dark (negative phase shift) because of the attractive interaction between the cantilever and the vortex. The reason why the vortex appears in this image and does not follow the moving cantilever despite the vortex-cantilever attraction is that at the present experimental conditions (temperature, lift, tip magnetization) the vortex pinning force by the sample exceeds its attraction by the cantilever, thus fixing the vortex position.

The MFM map presented in Fig. 1c was acquired at $T = 8.49$ K, that is 0.5 K below $T_c^{100\text{nm}}$, the same sample region as in Fig. 1b was explored. The overall gray background on this map corresponds to the positive phase shift, yet the gradient of the diamagnetic repulsion is slightly larger than in Fig. 1b, due to a lower cantilever lift $h = 80$ nm used (instead of 200 nm). On this map, no pinned vortex is visible anymore. Instead, a remarkable fish-skin-like pattern is observed with a nano-network of sharp dark boundaries where a strong attractive force is registered. Since the vortex is formed due to a topologically-protected phase singularity and cannot disappear, a tentative interpretation of this observation is that at these experimental conditions, the vortex gets unpinning and dragged by a scanning cantilever, thus exploring the pinning potential of the sample. In locations corresponding to phase drops, the moving cantilever exercises a stronger force to unpin and drag the vortex, and therefore, in these locations, the pinning is stronger. Thus, the phase shift maps of this Single-Quantum Vortex Microscopy reveal the spatial distribution of the pinning potential and its local strength (see Supplementary Fig. 3 for SQVM maps with two vortices). This is the central observation of the present work.

The geometry of SQVM is sketched in Fig. 1d; the theoretical justification of the approach is presented in Fig. 1e, f (see Section Modeling and Simulations in Methods for comprehensive details). At the superconducting transition, a vortex is created using the magnetic cantilever's stray field \mathbf{M} . The vortex has a core of the size of the thickness-dependent coherence length ξ_d ($\xi_d \sim 10$ – 20 nm in the studied films); the vortex supercurrents circulate around the core on the scale of the thickness-dependent magnetic penetration depth $\lambda_d > \xi_d$. The interaction force \mathbf{F} of such a vortex with the cantilever has a magnetic origin and can be seen as effectively attractive. Indeed, in the absence of the vortex, the magnetic flux from the oscillating cantilever is screened by the Meissner currents, resulting in a repulsion, while in the presence of a vortex, the vortex currents circulating in the direction opposite to the Meissner ones reduce the repulsion. The plot in Fig. 1e, obtained at the conditions close to the experimental ones in Fig. 1b,

depicts the free energy of the system as a function of the vortex location for fixed positions of the cantilever (in A) and the linear defect (in B). The energy is normalized to $E_0 = \Phi_0^2 / (64\pi^3 \lambda_d(0))$, where $\Phi_0 = ch/2e$ is the flux quantum, $\lambda_d(0)$ is the zero-temperature magnetic penetration depth taken equal to 130, 100 and 80 nm for $d = 50, 100,$ and 240 nm thick films, respectively⁵⁶. The free energy has a local minimum when the vortex is located below the cantilever. When the vortex moves away from A , the energy increases progressively on the lateral scale of the magnetic penetration depth, resulting in an increasing drag force F_{drag} , as presented in Fig. 1d. The other minimum exists at B when the vortex sits at the pinning defect. In the simulation (see Fig. 1e), the interaction that pins a vortex at the linear defect is stronger than the shallow minimum at the cantilever position in A . At this condition, the vortex remains strongly pinned at the defect, enabling its visualization in the MFM experiment, Fig. 1b. However, the temperature evolution of the two minima (at A and B) are different, as demonstrated in Fig. 1f. At low temperatures, the energy of the system with a vortex pinned at the linear defect B can indeed be significantly lower than the energy with the vortex under cantilever in A . Close enough to T_c the situation inverts. In terms of forces, it means that the maximum drag force of the tip now exceeds the pinning one. At this new condition, the scanning cantilever will unpin the vortex from the defect and drag it. This situation is realized in the SQVM experiment, Fig. 1c. The crossover temperatures T^* between the two regimes are presented by red open circles in Fig. 2h. The existence of T^* is confirmed experimentally (see Supplementary Fig. 4). Note that the simulations in Fig. 1f predict that the crossover temperature should depend on the film thickness.

The above considerations suggest that to enable the SQVM experiment, the vortex has to be unpinning from the defect and followed by the scanning cantilever. This requires the vortex-tip to have an effective, attractive interaction to exceed the pinning potential. The attraction can be increased by reducing the lift, while the pinning can be lowered by raising the temperature towards T_c . Indeed, the considerations behind the energy plots (Fig. 1e, f) take into account the vortex currents that circulate around the core and explore the disorder potential on the scale of the penetration depth λ_d as well as on the energy of the magnetic flux the currents create. Moreover, on the microscopic level, at least a part of the pinning potential is related to the energy E_{core} of the vortex core whose lateral size is of the order of ξ_d . This energy is positive, due to the suppression of the superconducting order parameter (the energy gap) $\Delta(r)$ inside the core: $E_{\text{core}} \sim N(E_F)\Delta^2 \times \xi_d^2 d$, where $\frac{1}{2}N(E_F)\Delta^2$ is the condensation energy density, $N(E_F)$ is the density of electronic states at the Fermi level E_F , and $\xi_d^2 d$ is the volume occupied by the core in the film. At a non-superconducting defect $\Delta(r) \rightarrow 0$ and, if the defect has a size $l \sim \xi_d$ and a substantial height $\sim d$, the energy E_{core} is reduced if the core coincides with the defect. That is why such defects (and particularly columnar ones) are usually strong vortex pinning centers. At $T \rightarrow T_c$ both $\xi_d, \lambda_d \rightarrow \infty$. Thus, close enough to T_c , the vortex core and the vortex currents occupy areas much larger than the size of individual defects; this “averaging over disorder” leads to the smearing of the pinning potential and to the consequent reduction of the pinning force, thus enabling the SQVM experiment in the temperature range $T^* < T < T_c$. In addition, thermal fluctuations and reduced Josephson inter-grain coupling also contribute to the depinning at higher temperatures.

To ensure that the network presented in Fig. 1c is indeed related to the Nb-film structure, further SQVM experiments were provided on Nb-films of different thicknesses. In Fig. 2a–c room-temperature topographic AFM images of the films are presented. They demonstrate the expected granular structure⁵⁵ and the well-known increase of the Nb-grain size with increasing film thickness⁵⁴. The superconducting properties of the films were characterized by four-probe electron transport; the results are presented in Fig. 2d (see Supplementary Fig. 6 for additional electron-transport characteristics of the films). The high film quality is witnessed by a high $T_c^{240\text{nm}} \approx 9.2$ K for a 240-nm-thick film; the expected slight decrease of T_c for thinner samples is also observed. The corresponding SQVM maps in Fig. 2e–g also show the same tendency: the characteristic spatial scales of the observed pinning network grow with the film thickness and thus clearly

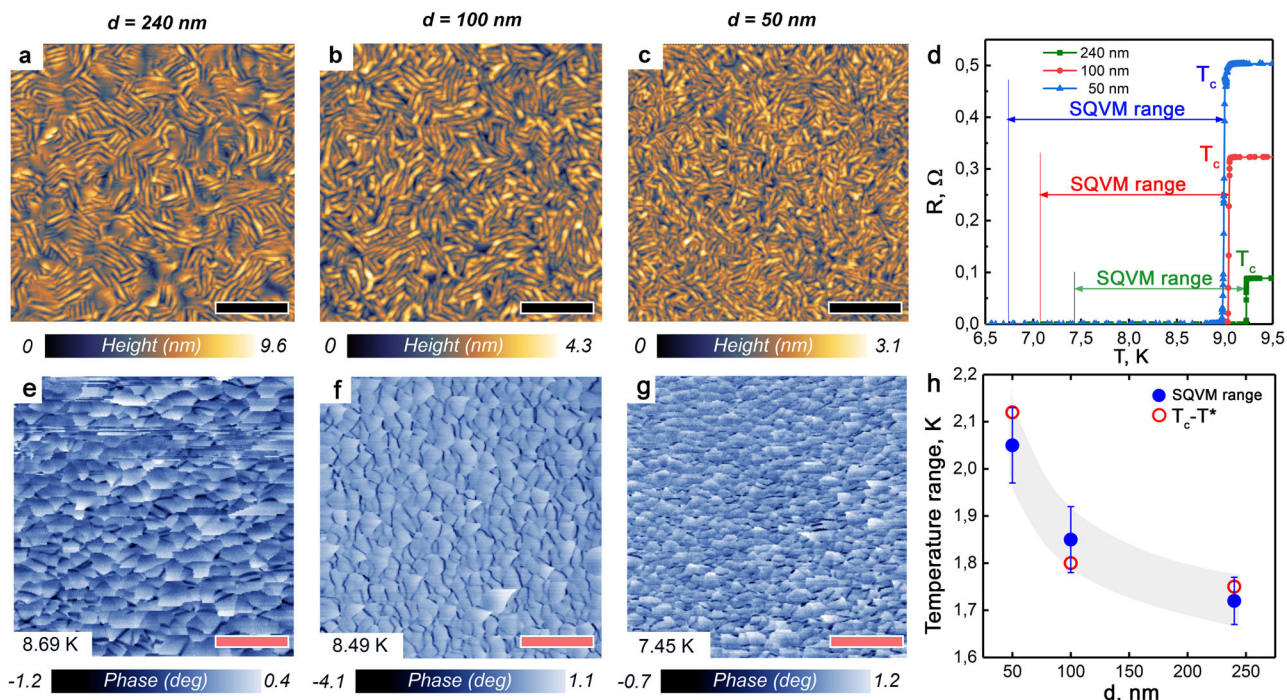


Fig. 2 | Thickness dependent vortex pinning network in Nb-films. a–c $1 \times 1 \mu\text{m}^2$ room-temperature AFM images of 240 nm, 100 nm, and 50 nm thick Nb films, respectively. The black bars correspond to 200 nm. Both grain size and apparent surface roughness increase with the film thickness. **d** Resistance of the films measured near the superconducting transition by the four-probe transport (refer to the Methods section concerning Transport measurements). For each thickness, colored arrows visualize the temperature range where SQVM experiment was enabled.

e–g $5 \times 5 \mu\text{m}^2$ SQVM maps (acquired at $h = 80$ nm) of the films showed in (a–c). The orange bars correspond to $1 \mu\text{m}$. **h** Blue circles: dependence of the SQVM temperature range on film thickness. Red open circles: calculated $T_c - T^*(d)$ (refer to the Methods section concerning Modeling and simulations). The error bars demonstrate the experimentally defined temperature uncertainty of T^* , arising due to the inhomogeneity of the pinning network, corresponding to $\sim \pm 0.05$ K.

correlate with the grain size. Notably, the observed spatial networks barely depend on temperature (see Supplementary Figs. 4 and 5), witnessing their direct relation to the film structure.

Discussion

We now discuss a deep connection of the SQVM to the film properties. We start with the analysis of the temperature range close to T_c where the SQVM experiments are enabled (shown by colored arrows in Fig. 2d and plotted as blue circles in Fig. 2h). Experimentally, the SQVM temperature range was found to vary significantly depending on film thickness: It gets wider with decreasing d (blue circles in Fig. 2h). Remarkably, this dependence almost perfectly coincides with the calculated $T_c - T^*(d)$, taking $T^*(d)$ from the numerical simulation presented in Fig. 1f. Note that the dependence is not trivial: to achieve a good agreement presented in Fig. 2h, calculations required accurately considering experimentally established thickness-dependent λ_d ⁵⁶. Therefore, by measuring the SQVM range and by inverting the used numerical protocol, it is possible to extract the effective ξ_d and λ_d . This is of high interest for ultra-thin superconducting films in which these characteristics are not straightforward to measure directly.

We now focus in more detail on the interaction of vortices with the cantilever – a key for understanding SQVM. In the experiment presented in Fig. 3a–c, we cooled a 240 nm thick film down to 4.07 K (that is well below its $T_c = 9.2$ K) in the presence of an external magnetic field $\vec{H} = 10$ Oe aligned with the stray field \vec{M} of the cantilever (Fig. 1d). On the phase map of Fig. 3a obtained at $T = 4.07$ K (that is well below the SQVM temperature range, Fig. 2d, h), several vortices are visible forming a disordered vortex lattice, as expected; all vortices have the same apparent size. The section of the phase map along the dashed line in Fig. 3a is presented as a blue curve in Fig. 3c. It demonstrates the “vortex size”, about 220 nm at half maximum (at 80 nm lift). Such a large value is due to the magnetic interaction between the vortex field laterally extending to $\sim \lambda_d$ and the cantilever field extending over hundreds of nanometers⁵⁷. At the same time, the cantilever oscillation

amplitude map presented in Fig. 3b is featureless (see also the section plot in Fig. 3c, red line). In fact, the cantilever oscillation amplitude is related to the dissipation in the coupled system vortex-cantilever^{39,40}. At the temperature of the experiment $\approx 0.4 T_c$, the theoretical curves in Fig. 3d obtained for different cantilever positions with respect to the vortex location – above the defect (blue line), at a distance of λ_d (green line), and $2\lambda_d$ (red line) – demonstrate that the cantilever is unable to unpin and drag vortices. Indeed, in all three cases, the minimum free energy remains at the position of the defect. The vortices remain pinned there and do not dissipate. That explains why the dissipation-related amplitude map in Fig. 3c is featureless.

The SQVM map taken at $T = 8.7$ K ($T \approx 0.9 T_c$) is presented in Fig. 3e. On this phase map, individual pinned vortex is not detected anymore but the pinning network is visible (similar to the result presented in Fig. 1c). In this case, sharp drops are also visible on the simultaneously recorded amplitude map, Fig. 3f; the position of the drops spatially coincide (the spatial correlation between amplitude and phase signals is clear in Fig. 3g). The calculations presented in Fig. 3h show that at this high temperature, the attraction by the cantilever exceeds the pinning force: the vortex gets unpinning and dragged, thus enabling SQVM experiment. The dissipation in the system vortex-cantilever varies upon the location of the vortex that explores the pinning landscape.

One of the puzzling features in the SQVM maps is therefore their surprising spatial sharpness: the phase drops occur on the scale ~ 15 – 30 nm (see plots in Fig. 3g). This is by far shorter than the characteristic scales of sample-cantilever magnetic interaction ($\lambda_d(T) \gtrsim 100$ nm, tip size, tip lift, etc.), which presumably would limit the spatial resolution of SQVM. To resolve the puzzle, one should recall the basic principles of MFM. The magnetic cantilever represents a mechanical mass-spring oscillator with the resonant frequency ω_0 . In the experiment, this oscillator is excited by a piezoelectric dizzier at a close frequency ω^{40} . The tip oscillates in the direction perpendicular to the surface; its position is $z = z_0 \cos(\omega t + \theta)$. In the presence of an external force with a non-zero z -component of the force

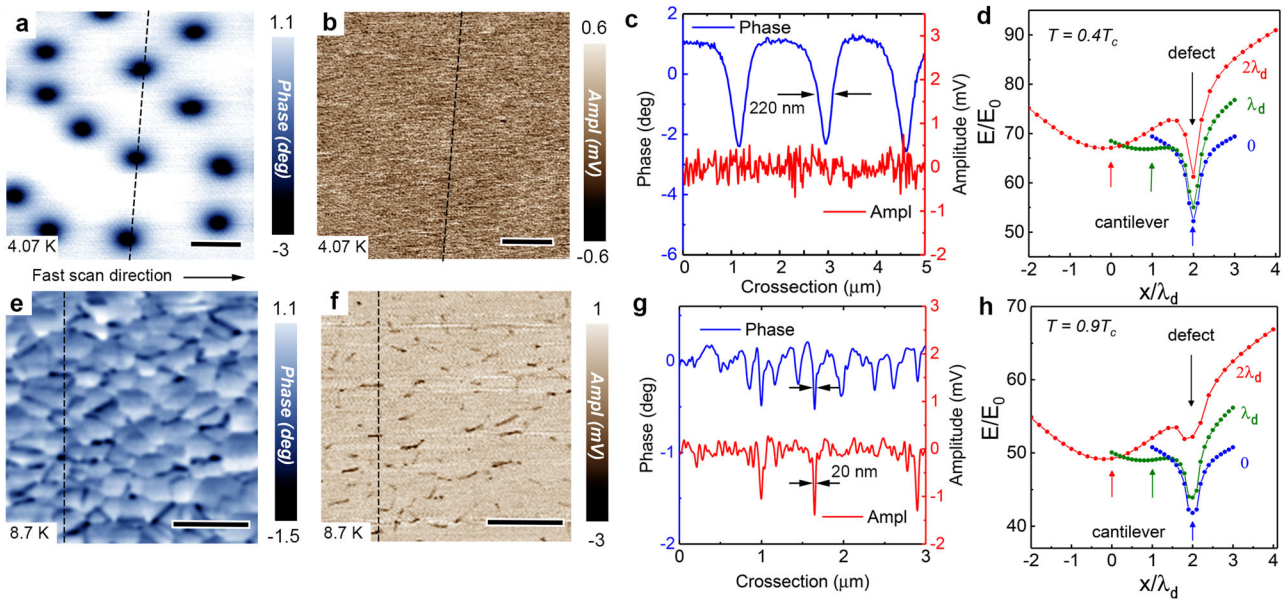


Fig. 3 | From pinned vortex MFM imaging to SQVM. $3 \times 3 \mu\text{m}^2$ MFM phase (a) and oscillation amplitude (b) maps acquired at $T = 4.07$ K and $h = 80$ nm in the 10 Oe field-cooled 240 nm thick Nb-film. c cross-section plots of the phase (blue curve) and oscillation amplitude (red curve) following the dashed lines in maps shown in (a, b). d calculated free energy at $0.4 T_c$ as a function of cantilever position (refer to the section on Modeling and Simulations in the Methods). e, f SQVM phase and

amplitude maps of the same sample acquired at $T = 8.7$ K and $h = 80$ nm. In this case, no external field was applied upon cooling. g a cross-section of the phase (blue curve) and amplitude (red curve) maps in (e, f). The black bars in (a, b, e, f) correspond to $1 \mu\text{m}$. h calculated free energy at $0.9 T_c$ as a function of cantilever position (refer to the section on Modeling and Simulations in the Methods).

gradient, the frequency ω , the oscillation amplitude z and the phase shift θ change by^{58,59}:

$$\delta\omega \approx -\frac{\omega}{2k} \frac{\partial F_z}{\partial z}, \quad \delta z \approx -\frac{2z_0 Q}{3\sqrt{3}k} \frac{\partial F_z}{\partial z}, \quad \delta\theta \approx -\frac{Q}{k} \frac{\partial F_z}{\partial z}, \quad (1)$$

where $Q = kz_0^2\omega_0/(2P_{\text{dis}})$ is the quality factor of the cantilever, and P_{dis} is the dissipated power. The vortex is strongly pinned at low temperatures, and the dissipation is low (no vortex core motion, no quasiparticles). At these conditions, the vortex appears in $\delta\theta(x, y)$ maps (as in Fig. 1b, for instance) due to the spatial variations of the force gradient $\frac{\partial F_z}{\partial z}$. When the cantilever apex is located away from a vortex, the interaction force F is mainly due to the repulsion by Meissner currents of the sample attempting to screen the stray magnetic field of the cantilever. Though, an attractive vortex-cantilever force dominates when the cantilever is situated close or above the vortex. Both vortex-generated and Meissner current-generated forces decay with increasing the cantilever-surface distance, but their directions are opposite, and thus, also are their gradients. That is why the phase shifts in Fig. 1b measured above the vortex and away from it have opposite signs. Note also that the attractive vortex-cantilever force is on the origin of the vortex drag when the tip is moved away from the vortex center. At low temperatures, this force does not exceed the pinning force; the vortex remains pinned enabling its imaging. The apparent vortex size of a few hundreds of nanometers (Figs. 1c, 3a, c results from the convolution of the lateral extend of the vortex field $\sim\lambda_d(4K) \approx 100 \text{ nm}$ ⁵⁶ with the magnetic footprint of the cantilever⁵⁷. When the temperature is increased, $\xi_d(T)$ and $\lambda_d(T)$ raise, the pinning force decreases and, at some temperature, becomes lower than the vortex-cantilever attraction. The vortex gets unpinned and can be dragged by the cantilever, as depicted in Fig. 1d. Close enough to T_c , vortex-cantilever attraction strongly dominates, and the vortex can be seen as rigidly “attached” to the scanning cantilever, while the vortex core and vortex currents interact with the local pinning network. At $T = 8.5$ K of the SQVM experiment presented in Fig. 1c, the vortex currents are already spread over large distances $\geq 2\lambda(8.5K) \sim 500 \text{ nm}$; they interact with a large number of local pinning centers (point defects, grain

boundaries, etc.). Therefore, at this temperature one does not expect sharp spatial variations in $\delta\theta(x, y)$ maps due to spatial variations of the vortex current distribution. However, the vortex core has a much smaller size $\sim\xi$ estimated to 15 nm at $T = 4 \text{ K}$ ⁶⁰, and to 38 nm at $T = 8.5 \text{ K}$. The core motion is dissipative; the dissipation depends on the normal state resistance of the material in the place occupied by the core. The grain boundaries are composed of disordered and partially oxidized Nb; the vortex core motion along and across these grain boundaries is more dissipative as compared to that in superconducting Nb. At such defects P_{dis} raises, the quality factor Q drops, resulting in sharp phase/amplitude shifts in SQVM maps. Local variations of P_{dis} are tiny but owing a very high Q -factor of the cantilever, $Q \sim 4000$, the detection of the vortex core motion is rather easy^{7,39,40,57}. Note that owing to the spatial sharpness of SQVM maps (Fig. 3g), the position of the pinning centers can be determined with a high accuracy $\sim 1 \text{ nm}$. This demonstrates a true nanoscale resolution of the SQVM we developed and used in this work.

In the present work, we studied standard magnetron-sputtered Nb-films which are commonly used in superconducting technology such as rapid single flux quantum electronics, qubits, shift registers, sensors, etc. In these applications, the precise knowledge of local superconducting properties is strongly desired. With this respect, the implemented SQVM is a powerful tool as it provides direct information on vortex pinning with a nano-scale resolution limited by the superconducting coherence length; in commonly used type-II superconductors (Nb, NbN, TiN,...) the latter is much shorter than the magnetic penetration depth. For the studied sputtered thin Nb-films, the SQVM shows that there is no direct correlation between the granular structure of the films and their local superconducting properties, and thus, the knowledge of the film morphology is not enough to decide on superconducting properties. This is because surface-sensitive methods such as SEM, STM, AFM, etc. provide no input about the inter-grain coupling in the bulk, which is crucial for superconductivity. The macroscopic transport experiments do provide some input through the critical current and critical field measurements. Though these results are difficult to connect directly to the superconducting properties on the local scale.

Conclusion

To conclude, we revealed the vortex pinning nano-network in thin superconducting films made of sputtered Nb. In the heart of the experiment is a scanning probe microscopy approach that we named Scanning Quantum Vortex Microscopy. The method is based on creating, attracting, and dragging a single quantum vortex by the tip of a MFM. The interaction of the moving vortex with defects present in the sample leads to an additional location-dependent pinning force and related dissipation that both modify the amplitude and phase of the oscillating MFM cantilever. These characteristics are measured in the experiment and are presented as maps. Since the vortex pinches through the total thickness of a superconductor, it probes both the surface and the bulk components of the pinning potential. Recorded maps of the phase variations can be considered as a projection onto the scanning plane of hidden grain boundaries and other types of extended defects pinning vortices inside the superconducting film. We demonstrated the SQVM to enable visualization of defects in superconducting films with a nm resolution over a large field of view. This opens unparalleled possibilities for detailed non-destructive studies of defects inside superconductors and superconducting nano-devices.

Methods

Sample preparation

Nb-films were fabricated using 2-inch UHV magnetron sputtering. 50, 100, and 240 nm Nb films were deposited onto SiO₂(270 nm)/Si(100) substrate; the following parameters were used: pre-etching in Ar plasma $t_{etch} = 180$ s, $p^{Ar} = 2 \cdot 10^{-2}$ mbar, $P_{RF} = 80$ W at $V_{dc} = 580$ V, deposition $P_{RF} = 200$ W at $V_{dc} = 238$ V, $p^{Ar} = 4 \times 10^{-3}$ mbar, deposition rate 0.22 nm/s.

Transport measurements

Electron transport measurements were conducted using a standard four-probe setup in the system Attocube Attodry 1000/SU.

High resolution AFM measurements

The high-resolution topographic images were acquired under ambient conditions using the PeakForce method on the Bruker Multimode V8 Atomic Force Microscope and using a non-magnetic Ostek HA_CNC cantilever with a stiffness constant of $k = 1.5$ N/m.

Cryogenic MFM and SQVM measurements

MFM studies at low temperatures were conducted using the AttoCube AttoDry 1000/SU system, equipped by a 9 T superconducting magnet. All MFM measurements were provided in the temperature range from 4 to 30 K; the samples were placed in an environment of helium exchange gas (pressure of 0.5 mbar @ 300 K). During the experiments, the temperature was controlled within 1 mK. Standard Co/Cr-coated magnetic cantilevers (MESP, Bruker) with a 2.8 N/m spring constant were used. Prior to the experiments, the probes were magnetized at 30 K with a magnetic field of 2 kOe. The phase contrast was detected in the non-contact mode.

Modeling and simulations

In order to support our interpretation of the experimentally observed features, we consider a simple model problem of the vortex pinning by a planar defect in a thin superconducting film of the thickness $d \ll \lambda_L(0)$, where $\lambda_L(0)$ is the London penetration depth at zero temperature. In this limit, the screening properties of the film are determined by the temperature-dependent Pearl length $\lambda_d = \lambda_L^2(T)/d = \lambda_d(0)/(1 - T^4/T_c^4)^{51}$, where $\lambda_d(0)$ is assumed to reduce slightly as the film thickness increases. To model the vortex pinning, we introduce a high $-j_c$ planar defect described by a standard Josephson current-phase relation $j = j_c \sin \varphi$. The temperature dependence of the critical current density j_c of a granular superconductor, modeled as an array of Josephson-coupled grains, is described by the

Ambegaokar-Baratoff relation⁶²

$$j_c = j_0 \frac{|\Delta(T)|}{|\Delta(0)|} \tanh\left(\frac{|\Delta(T)|}{2k_B T}\right) \quad (2)$$

with the BCS-like dependence of the superconducting order parameter $\Delta(T)$. Here, the free parameter j_0 determines the scale of the elementary pinning force.

A MFM tip is modeled by a point magnetic charge Q which is positioned at a height h above the film and is shifted in the lateral direction at the distance t with respect to the linear defect^{57,59}. In the absence of a superconducting film, the stray magnetic field of the tip $\mathbf{B}^Q = \text{curl } \mathbf{A}^Q$ is described by the vector potential $\mathbf{A}^Q = A^Q(r, z) \mathbf{e}_\theta$

$$A^Q(r, z) = \frac{Q}{4\pi r} \left(1 + \frac{z-h}{\sqrt{r^2 + (z-h)^2}} \right), \quad (3)$$

where (r, θ, z) is the polar coordinate system. We assume here that the density of the induced supercurrent $\mathbf{j}(\mathbf{r})$ is so weak that the suppression of the magnitude of the superconducting order parameter is negligible everywhere in the film except for the vortex core. The sheet current $\mathbf{g}(\mathbf{r}) = \mathbf{j}(\mathbf{r}) \cdot d$, averaged over the film thickness induces the magnetic field $\mathbf{B} = \text{curl } \mathbf{A}$ according to the Maxwell equation:

$$\text{curl curl } \mathbf{A} = \frac{4\pi}{c} \mathbf{g}(\mathbf{r}), \quad (4)$$

where

$$\mathbf{g}(\mathbf{r}) = \frac{c}{4\pi\lambda_d} (\mathbf{S}^P + \mathbf{S}^D - \mathbf{A} - \mathbf{A}^Q) \delta(z). \quad (5)$$

Here the term \mathbf{S}^P describes the vortex source at the point $\mathbf{r}_0 = (x_0, y_0)^{61}$

$$\text{curl } \mathbf{S}^P = \Phi_0 \delta(\mathbf{r} - \mathbf{r}_0) \mathbf{z}_0, \quad (6)$$

while the term \mathbf{S}^D accounts for the planar defect at $x = t$ with the order-parameter phase difference $\varphi(y)^{63}$

$$\text{curl } \mathbf{S}^D = \frac{\Phi_0}{2\pi} \frac{d\varphi}{dy} \delta(x-t) \mathbf{z}_0, \quad (7)$$

$\mathbf{r} = (x, y)$ is the lateral coordinate, and $\Phi_0 = \pi\hbar c/e$ is the flux quantum. For an arbitrary position (x_0, y_0) of the vortex with respect to the MFM tip and the planar defect and for a given phase difference $\varphi(y)$, the linear equations (3)–(7) can be solved by the standard Fourier method.

To obtain a self-consistent equation for the phase difference $\varphi(y)$ we use the boundary condition for the normal component of the sheet current $g_x(x, y)|_{x=t}$ flowing through the planar defect

$$g_x(t, y) = g_c \sin \varphi(y), \quad (8)$$

where $g_c = j_c \cdot d$ is the critical current of the edge junction in the thin film. The magnetic field induced by the cantilever \mathbf{B}^Q and the Pearl vortex trapped in one of the banks of an edge-type planar junction cause an extra phase difference on the junction that depends on both an inhomogeneous magnetic field of the probe^{40,64} and the vortex positions with respect to the defect^{65–69}. The Josephson effect at such edge junction is quite different from those at familiar bulk junctions, because the stray magnetic field results in an integral equation governing the phase distribution $\varphi(y)$, i.e., the problem becomes non-local^{63,70}. The edge Josephson junction in the thin film is characterized by two temperature-dependent characteristic lengths. The first one is the Pearl length λ_d which describes the magnetic field screening

by thin superconducting film. Another parameter is the length L characterizing the junction properties

$$L = \frac{\lambda_J^2}{\lambda_L} = \frac{c\Phi_0}{16\pi^2 g_c \lambda_d}, \quad (9)$$

where $\lambda_J = \sqrt{c\Phi_0/16\pi^2 j_c \lambda_L}$ is so-called Josephson length. Using the boundary condition (8) and the solution of the Eqs. (3)-(7) one finally obtains the following integral equation for the order parameter phase difference $\varphi(y)$

$$\lambda_d \int_{-\infty}^{\infty} ds \varphi_s''(s) G_0(0, y-s) = \mu \sin \varphi(y) - \frac{4Qy}{\Phi_0 \sqrt{y^2 + t^2}} \int_0^{\infty} dq \frac{q J_1(q \sqrt{y^2 + t^2} / \lambda_d) e^{-qh/\lambda_d}}{1+2q} + \frac{\pi(y-y_0)}{\sqrt{(y-y_0)^2 + (t-x_0)^2}} G_1(t-x_0, y-y_0), \quad (10)$$

where the dimensionless parameter $\mu = 2\lambda_d/L$ depends on temperature T , and two auxiliary functions

$$G_0(u, v) = H_0\left(\frac{\sqrt{u^2 + v^2}}{2\lambda_d}\right) - Y_0\left(\frac{\sqrt{u^2 + v^2}}{2\lambda_d}\right), \quad (11)$$

$$G_1(u, v) = H_1\left(\frac{\sqrt{u^2 + v^2}}{2\lambda_d}\right) - Y_1\left(\frac{\sqrt{u^2 + v^2}}{2\lambda_d}\right) - \frac{2}{\pi}.$$

can be expressed via Struve functions H_0 and H_1 of zero and first orders, and second-kind Bessel functions Y_0 and Y_1 of zero and first orders. At zero temperature the μ parameter is equal to $\mu(0) = 32\pi^2 j_0 \lambda_d(0)^2 d / (c\Phi_0)$. The equation (10) was solved numerically using the iteration method on a discrete grid of nodes with a step $\Delta y = 0.005\lambda_d$ and the accuracy better than 10^{-5} . The total energy $E = E_J + E_g + E_B$ of the system under consideration consists of the Josephson coupling energy (E_J), the kinetic energy (E_g) of the supercurrents, and the energy of stray magnetic field (E_B) in the surrounding space:

$$E = \frac{\Phi_0^2}{32\pi^3 \lambda_d L} \int dy [1 - \cos \varphi(y)] + \frac{2\pi\lambda_d}{c^2} \int d\mathbf{r} \mathbf{g}^2(\mathbf{r}) + \frac{1}{8\pi} \int d\mathbf{r} dz \mathbf{B}^2, \quad (12)$$

We performed numerical calculations of the free energy (12) as a function of a vortex position (x_0, y_0) for different values of temperature T , the lift of the cantilever h and the shift of the cantilever with respect to the defect t taking a fixed value of $\mu(0) = 0.32$ (see panels e-f in Fig. 1 and panels d-h in Fig. 3).

Data availability

Authors can confirm that all relevant data are included in the paper and its supplementary information files. Additional data are available on request from the authors.

Received: 19 March 2024; Accepted: 17 February 2025;

Published online: 04 March 2025

References

- Ménard, G. C. et al. Coherent long-range magnetic bound states in a superconductor. *Nat. Phys.* **11**, 1013 (2015).
- Aladyshkin, A. Y., Silhanek, A. V., Gillijns, W. & Moshchalkov, V. V. Nucleation of superconductivity and vortex matter in superconductor-ferromagnet hybrids (topical review). *Supercond. Sci. Technol.* **22**, 053001 (2009).
- Vagov, A. et al. Intertype superconductivity in ferromagnetic superconductors. *Commun. Phys.* **6**, 284 (2023).

- Gershenzon, M. E. & Koshelets, V. P. Superconductive properties of niobium and niobium nitride films made by high-frequency cathode sputtering. *Zh. Tekh. Fiz.* **50**, 572–576 (1980).
- Sung, Z.-H., Lee, P. J., Gurevich, A. & Larbalestier, D. C. Evidence for preferential flux flow at the grain boundaries of superconducting RF-quality niobium. *Supercond. Sci. Technol.* **31**, 045001 (2018).
- Golod, T. et al. Reconfigurable Josephson phase shifter. *Nano Lett.* **21**, 5240 (2021).
- Grebenchuk, S. Y., Hovhannisyán, R., Shishkin, A., Dremov, V. & Stolyarov, V. Magnetic force microscopy for diagnosis of complex superconducting circuits. *Phys. Rev. Appl.* **18**, 054035 (2022).
- Hovhannisyán, R. A., Golod, T. & Krasnov, V. M. Controllable manipulation of semifluxon states in phase-shifted Josephson junctions. *Phys. Rev. Lett.* **132**, 227001 (2024).
- Golovchanskiy, I. A., Pan, A. V., Shcherbakova, O. V. & Fedoseev, A. A. Rectifying differences in transport, dynamic, and quasi-equilibrium measurements of critical current density. *J. Appl. Phys.* **114**, 163910 (2013).
- Golovchanskiy, I. A., Pan, A. V., Fedoseev, S. A. & Higgins, M. Significant tunability of thin film functionalities enabled by manipulating magnetic and structural nano-domains. *Appl. Surf. Sci.* **311**, 549 (2014).
- Annunziata, A. J. et al. Tunable superconducting nanoinductors. *Nanotechnology* **21**, 445202 (2010).
- Carbillet, C. et al. Spectroscopic evidence for strong correlations between local superconducting gap and local Altshuler-Aronov density of states suppression in ultrathin NbN films. *Phys. Rev. B* **102**, 024504 (2020).
- Soloviev, I. I. et al. Superconducting circuits without inductors based on bistable Josephson Junctions. *Phys. Rev. Appl.* **16**, 014052 (2021).
- Blatter, G., Feigel'man, M. V., Geshkenbein, V. B., Larkin, A. I. & Vinokur, V. M. Vortices in high-temperature superconductors. *Rev. Mod. Phys.* **66**, 1125 (1994).
- Berdiyrov, G. R., Milošević, M. V. & Peeters, F. M. Vortex configurations and critical parameters in superconducting thin films containing antidot arrays: Nonlinear Ginzburg-Landau theory. *Phys. Rev. B* **74**, 174512 (2006).
- Berdiyrov, G. R., Milošević, M. V. & Peeters, F. M. Composite vortex ordering in superconducting films with arrays of blind holes. *N. J. Phys.* **11**, 013025 (2009).
- Willa, R., Koshelev, A. E., Sadovskyy, I. A. & Glatz, A. Strong-pinning regimes by spherical inclusions in anisotropic type-II superconductors. *Supercond. Sci. Technol.* **31**, 014001 (2018).
- Samokhvalov, A. V. et al. Properties of Josephson junctions in the nonuniform field of ferromagnetic particles. *JETP Lett.* **95**, 104–113 (2012).
- Kwok, W.-K. et al. Vortices in high-performance high-temperature superconductors. *Rep. Prog. Phys.* **79**, 116501 (2016).
- Bean, C. P. & Livingston, J. D. Surface barrier in type-II superconductors. *Phys. Rev. Lett.* **12**, 14 (1964).
- Daldini, O., Martinoli, P., Olsen, J. L. & Berner, G. Vortex-Line pinning by thickness modulation of superconducting films. *Phys. Rev. Lett.* **32**, 218 (1974).
- Crisan, A., Fujiwara, S., Nie, J. C., Sundaresan, A. & Ihara, H. Sputtered nanorods: a costless method for inducing effective pinning centers in superconducting thin films. *Appl. Phys. Lett.* **79**, 4547 (2001).
- Van Bael, M. J., Temst, K., Moshchalkov, V. V. & Bruynseraede, Y. Pinning by an antidot lattice: the problem of the optimum antidot size. *Phys. Rev. B* **59**, 14674 (1999).
- Feighan, J. P. F., Kursumovic, A. & MacManus-Driscoll, J. L. Materials design for artificial pinning centres in superconductor PLD coated conductors. *Supercond. Sci. Technol.* **30**, 123001 (2017).

25. Bugoslavsky, Y. et al. Enhancement of the high-magnetic-field critical density of superconducting MgB₂ by proton irradiation. *Nature* **411**, 561 (2001).
26. Devred, A. Practical low-temperature superconductors for electromagnets, *CERN Rep.* **4**, <https://doi.org/10.5170/CERN-2004-006> (2004).
27. Golovchanskiy, I. et al. Magnetization dynamics in proximity-coupled superconductor-ferromagnet-superconductor multilayers. II. Thickness dependence of the superconducting torque. *Phys. Rev. Appl.* **19**, 034025 (2023).
28. Martinez, E. et al. Microstructures of niobium components fabricated by electron beam melting. *Metallogr., Microstruct. Anal.* **2**, 183 (2013).
29. Stolyarov, V. S. et al. Expansion of a superconducting vortex core into a diffusive metal. *Nat. Commun.* **9**, 2277 (2018).
30. Berti, G. et al. Scanning tunneling microscopy and spectroscopy characterization of Nb films for quantum applications. *Appl. Phys. Lett.* **122**, 192605 (2023).
31. Wu, G. et al. Studies of niobium thin film produced by energetic vacuum deposition. *Thin Solid Films* **489**, 56 (2005).
32. Veshchunov, I. S. et al. Optical manipulation of single flux quanta. *Nat. Commun.* **7**, 12801 (2016).
33. Harada, K. et al. Real-time observation of vortex lattices in a superconductor by electron microscopy. *Nature* **360**, 51 (1992).
34. Vinnikov, L. Y., Veshchunov, I. S., Sidelnikov, M. S. & Stolyarov, V. S. The high-resolution bitter decoration technique for the magnetic flux structure imaging at low temperatures. *Instrum. Exp. Tech.* **62**, 587–593 (2019).
35. Embon, L. et al. Imaging of super-fast dynamics and flow instabilities of superconducting vortices. *Nat. Commun.* **8**, 85 (2017).
36. Halbertal, D. et al. Nanoscale thermal imaging of dissipation in quantum systems. *Nature* **539**, 407 (2016).
37. Ge, J.-Y., Gutierrez, J., Gladilin, V. N., Devreese, J. T. & Moshchalkov, V. V. Bound vortex dipoles generated at pinning centres by Meissner current. *Nat. Commun.* **6**, 6573 (2015).
38. Auslaender, O. M. et al. Mechanics of individual isolated vortices in a cuprate superconductor. *Nat. Phys.* **5**, 35 (2009).
39. Stolyarov, V. S. et al. Revealing Josephson vortex dynamics in proximity junctions below critical current. *Nano Lett.* **22**, 5715 (2022).
40. Dremov, V. V. et al. Local Josephson vortex generation and manipulation with a magnetic force microscope. *Nat. Commun.* **10**, 4009 (2019).
41. Stolyarov, V. S. et al. Domain Meissner state and spontaneous vortex-antivortex generation in the ferromagnetic superconductor *EuFe₂(As_{0.79}P_{0.21})₂*. *Sci. Adv.* **4**, eaat1061 (2018).
42. Werner, R. et al. Domain-wall and reverse-domain superconducting states of a Pb thin-film bridge on a ferromagnetic BaFe₁₂O₁₉ single crystal. *Phys. Rev. B* **84**, 020505(R) (2011).
43. Galin, M. A. et al. Direct visualization of phase-locking of large Josephson junction arrays by surface electromagnetic waves. *Phys. Rev. Appl.* **14**, 024051 (2020).
44. Rosticher, M. et al. A high efficiency superconducting nanowire single electron detector. *Appl. Phys. Lett.* **97**, 183106 (2010).
45. Clem, J. R. & Huebener, R. P. Application of low-temperature scanning electron microscopy to superconductors. *J. Appl. Phys.* **51**, 2764 (1980).
46. Ciovati, G. et al. Low temperature laser scanning microscopy of a superconducting radio-frequency cavity. *Rev. Sc. Instr.* **83**, 034704 (2012).
47. Park, G. S., Cunningham, C. E., Cabrera, B. & Huber, M. E. Vortex pinning force in a superconducting niobium strip. *Phys. Rev. Lett.* **68**, 1920 (1992).
48. DasGupta, A., Koch, C. C., Kroeger, D. M. & Chou, Y. T. Flux pinning by grain boundaries in niobium bicrystals. *Philos. Mag. B* **38**, 367–380 (1978).
49. Skryabina, O. V. et al. Josephson coupling across a long single-crystalline Cu nanowire. *Appl. Phys. Lett.* **110**, 222605 (2017).
50. Bannykh, A. A. et al. Josephson tunnel junctions with a strong ferromagnetic interlayer. *Phys. Rev. B* **79**, 054501 (2009).
51. Werner, R. et al. Edge superconductivity in Nb thin film microbridges revealed by electric transport measurements and visualized by scanning laser microscopy. *Supercond. Sci. Technol.* **26**, 095011 (2013).
52. Pinto, N. et al. Dimensional crossover and incipient quantum size effects in superconducting niobium nanofilms. *Sci. Rep.* **8**, 4710 (2018).
53. Zikiy, E. V. et al. Mutual control of critical temperature, RRR, stress, and surface quality for sputtered Nb films. arXiv preprint arXiv:2502.03299 (2025).
54. Jin, Y., Song, X. & Zhang, D. Grain-size dependence of superconductivity in dc sputtered Nb films. *Sci. China Ser. G Phys. Mech. Astron.* **52**, 1289–1292 (2009).
55. Li, X. et al. Structural and nanomechanical characterization of niobium films deposited by DC magnetron sputtering. *Appl. Phys. A* **122**, 1–6 (2016).
56. Gubin, A. I., Il'in, K. S., Vitusevich, S. A., Siegel, M. & Klein, N. Dependence of magnetic penetration depth on the thickness of superconducting Nb thin films. *Phys. Rev. B* **72**, 064503 (2005).
57. Hovhannisyan, R. A., Grebenchuk, S. Y., Baranov, D. S., Roditchev, D. & Stolyarov, V. S. Lateral Josephson junctions as sensors for magnetic microscopy at nanoscale. *J. Phys. Chem. Lett.* **12**, 12196 (2021).
58. Fraerman, A. A. et al. Observation of MFM tip-induced remagnetization effects in elliptical ferromagnetic nanoparticles. *Phys. Low. Dim. Struct.* **1/2**, 117–122 (2004).
59. Di Giorgio, C. et al. Quantitative magnetic force microscopy using calibration on superconducting flux quanta. *Nanotechnology* **30**, 314004 (2019).
60. Zeinali, A., Golod, T. & Krasnov, V. M. Surface superconductivity as the primary cause of broadening of superconducting transition in Nb films at high magnetic fields. *Phys. Rev. B* **94**, 214506 (2016).
61. Pearl, J. Current distribution in superconducting films carrying quantized fluxoids. *Appl. Phys. Lett.* **5**, 65 (1964).
62. Ambegaokar, V. and Baratoff, A. Tunneling Between Superconductors. *Phys. Rev. Lett.* **10**, 486 (1963).
63. Kogan, V. G., Dobrovitski, V. V., Clem, J. R., Mawatari, Y. & Mints, R. G. Josephson junction in a thin film. *Phys. Rev. B* **63**, 144501 (2001).
64. Samokhvalov, A. V. Maximal supercurrent of a Josephson junction in a field of magnetic particles. *JETP Lett.* **78**, 3691 (2003).
65. Kogan, V. G. & Mints, R. G. Interaction of Josephson junction and distant vortex in narrow thin-film superconducting strips. *Phys. Rev. B* **89**, 014516 (2014).
66. Mironov, S. et al. Anomalous Josephson effect controlled by an Abrikosov vortex. *Phys. Rev. B* **96**, 214515 (2017).
67. Aslamazov, L. G. & Gurovich, E. V. Pinning of solitons by Abrikosov vortices in distributed Josephson junctions. *Pisma Zh. Eksp. Teor. Fiz.* **40**, 22 (1984).
68. Fistul, M. V. & Giuliani, G. F. Critical current of a long Josephson junction in the presence of a perturbing Abrikosov vortex. *Phys. Rev. B* **58**, 9343 (1998).
69. Golod, T., Rydh, A. & Krasnov, V. M. Detection of the phase shift from a single Abrikosov Vortex. *Phys. Rev. Lett.* **104**, 227003 (2010).
70. Ivanchenko, Yu. M. & Soboleva, T. K. Nonlocal interaction in Josephson junctions. *Phys. Lett. A* **147**, 65 (1990).

Acknowledgements

The authors thank Prof. V. M. Krasnov for the assistance with manuscript preparation. The MFM experiments were carried out with the support of the Russian Science Foundation project No. 23-72-30004. The samples were elaborated with the support of a grant from the Ministry of Science and

Higher Education of the Russian Federation, No. 075-15-2024-632. D.R. and V.S.S acknowledge “Bourses Metchnikov - séjours scientifiques” 2023 and 2024.

Author contributions

V.S.S. suggested the idea of the experiment; V.S.S. conceived the project and supervised the experiments; A.G.Sh., O.V.S., and V.S.S. performed the sample and surface preparation for MFM experiments; A.K.G. performed high-resolution AFM measurements; R.A.H., S.Yu.G., S.A.L., V.V.D., and V.S.S. performed cryogenic MFM measurements. R.A.H., S.A.L., N.E.K., E.A.D., I.A.G., A.Yu.A., and V.S.S. performed numerical analysis of the MFM and SQVM data; D.R. and V.S.S. provided the explanation of the observed effects; A.S.M. and A.V.S. did numerical modeling; D.R. and V.S.S. wrote the manuscript with the essential contributions from other authors; D.R. acknowledges French ANR grant CRYSTOP.

Competing interests

The authors declare no competing interests.

Additional information

Supplementary information The online version contains supplementary material available at <https://doi.org/10.1038/s43246-025-00759-6>.

Correspondence and requests for materials should be addressed to Vasily S. Stolyarov.

Peer review information *Communications Materials* thanks Martino Poggio and the other, anonymous, reviewer(s) for their contribution to the peer review of this work. Primary Handling Editors: Nicola Poccia and Aldo Isidori.

Reprints and permissions information is available at <http://www.nature.com/reprints>

Publisher's note Springer Nature remains neutral with regard to jurisdictional claims in published maps and institutional affiliations.

Open Access This article is licensed under a Creative Commons Attribution-NonCommercial-NoDerivatives 4.0 International License, which permits any non-commercial use, sharing, distribution and reproduction in any medium or format, as long as you give appropriate credit to the original author(s) and the source, provide a link to the Creative Commons licence, and indicate if you modified the licensed material. You do not have permission under this licence to share adapted material derived from this article or parts of it. The images or other third party material in this article are included in the article's Creative Commons licence, unless indicated otherwise in a credit line to the material. If material is not included in the article's Creative Commons licence and your intended use is not permitted by statutory regulation or exceeds the permitted use, you will need to obtain permission directly from the copyright holder. To view a copy of this licence, visit <http://creativecommons.org/licenses/by-nc-nd/4.0/>.

© The Author(s) 2025